INTERNATIONAL JOURNAL OF
NUMERICAL ANALYSIS AND MODELING
Volume 7, Number 1, Pages 173–193

DNS OF FORCED MIXING LAYER

MOHAMMAD JAVAD MAGHREBI AND AHAD ZARGHAMI

(Communicated by Jie Shen)

Abstract. The non-dimensional form of Navier-Stokes equations for two dimensional mixing layer flow are solved using direct numerical simulation. The governing equations are discretized in streamwise and cross stream direction using a sixth order compact finite difference scheme and a mapped compact finite difference method, respectively. A tangent mapping of $y = \beta \tan(\pi\zeta/2)$ is used to relate the physical domain of y to the computational domain of ζ. The third order Runge-Kutta method is used for the time-advancement purpose. The convective outflow boundary condition is employed to create a non-reflective type boundary condition at the outlet. An inviscid (Stuart flow) and a completely viscous solution of the Navier-Stokes equations are used for verification of the numerical simulation. The numerical results show a very good accuracy and agreement with the exact solution of the Navier-Stokes equation. The results of mixing layer simulation also indicate that the time traces of the velocity components are periodic. Results in self-similar coordinate were also investigated which indicate that the time-averaged statistics for velocity, vorticity, turbulence intensities and Reynolds stress distribution tend to collapse on top of each other at the flow downstream locations.

Key Words. Mixing Layer, Compact Finite Difference, Mapped Finite Difference, Self-Similarity.

1. Introduction

The plane mixing layer is characterized by the merging of two co-flowing fluid streams with different velocities. Typically, the two streams are separated by an impermeable object upstream of the confluence of these streams. This situation is illustrated in Fig1 [1]. Downstream of the confluence, the two streams exchange momentum as they come into intimate contact with each other. The mixing layer itself is defined by the region in which this merging process is occurring. Being such a simple configuration, it stands to reason that the mixing layer is one of the more common flows experienced in nature. Mixing layer are encountered in many application such as combustion furnaces, chemical lasers, the lip of an intake valve in an internal combustion engine and the trailing edge of a turbine blade.
Schlichting [2] shows that the boundary layer equations are valid for mixing layer at high Reynolds number. He assumed that two initially unperturbed parallel flow streams with velocities U, λU interact as a consequence of friction with one another from the position $x = 0$ to downstream. For the low values of viscosity ν, the transition from the velocity U to the velocity λU takes place in a thin mixing zone, in which the transverse component v of the velocity is small in compare with the longitudinal velocity component u. This boundary layer equation without the

Received by the editors April 8, 2008 and, in revised form, February 17, 2009.

presence of pressure gradient term is valid. Since there is no characteristic length in this problem, similar solutions are found.

Perhaps the first major experimental investigation of the mixing layer was undertaken by Liepmann and Laufer [3]. Many of the statistical quantities were explored in this investigation. Brown and Roshko [4] performed a study on density effects in the mixing layer which would lay the groundwork for a virtual revolution in turbulence. Mungal and Dimotakis [5] considered the mixing and combustion of two reactants in a gaseous mixing layer.

With advent of large scale computers, there has been a veritable explosion of numerical work done in concert with the experiments in an effort to understand the physics of mixing layer. Generally, there are two advanced methods of computing turbulent flow: large eddy simulation (LES) and direct numerical simulation (DNS).

In LES, a low-pass spatial filtering is applied to the Navier-Stokes equation and the filtered equations are solved directly. It is most promising for engineering flow of low-to-moderate Reynolds numbers [6], [7]. A review of LES for incompressible flow can be found in [8].

The main purpose of DNS is to solve (to best of our ability) for the turbulent velocity field without the use of turbulent modeling. This condition means that the Navier-Stokes momentum equation for fluid must be solved exactly, which is not a simple task [9], [10]. Thus, any DNS code is very time consuming and the extensive storage requirements. The DNS requires a large number of grid points and time steps to reach a statistically steady state and are usually limited to relatively low Reynolds numbers. With the advantage of powerful super computers, numerical simulation have become a viable tool for investigating mixing layer flows such as high speed mixing layer [11], particle laden mixing layer [12] and mixing layer with chemical reaction [13], [14].

In this paper the governing equations are derived from the full incompressible Navier-Stocks equations. These are solved in a domain which is finite in the streamwise direction, x and doubly infinite in the cross stream direction of y. In the x direction a high order compact finite difference scheme is used. In the y direction, a mapped compact finite difference method is employed. All quantities are nondimensionalized by the appropriate characteristic scales of the nixing layer flow. Specially, all lengths are normalized by the vorticity thickness of the reference velocity profile, δ_{ω_0}. Velocities are normalized by free streams streamwise velocity difference ΔU, where $\Delta U = U_1 - U_2$ and those pertaining to time are normalized by $\delta_{\omega_0}/\Delta U$.

The mean component of the streamwise velocity at the inlet plane of the domain, termed "reference" velocity also, is represented by:

$$U_0(y) = \frac{1}{2}\left\{\left(1/\lambda\right) + \tanh(2y)\right\}. \tag{1}$$

where the aforementioned normalization has been incorporated. The parameter $\lambda = [U_1 - U_2]/[U_1 + U_2]$ represents a measure for the intensity of shearing of the layer. The value of 2 in the argument for the tanh is required to make the vorticity thickness of this profile consistent with the implicit normalization of z on δ_{ω_0}.

2. The Governing Equations

Figure (1) shows the coordinate system and the computational domain in which the governing equations for the incompressible mixing layer flow are solved. The

inlet mixing profile is specified by $U_0(y)$ that has a superimposed computational velocity. The mixing layer flow is allowed to develop in the spatial direction x.
Applying Newton's second low of motion for a Newtonian fluid particle gives the equation of motion, known as the Navier-Stokes equations. These equations together with an equation representing mass conservation are the governing equation for an incompressible mixing layer flow.
The governing equations (Eq. (2) and Eq. (3)) have been non-dimensionalized by the characteristic length (δ_{ω_0}) and velocity scales (ΔU).

$$\frac{\partial \vec{U}}{\partial t} + (\vec{U}.\nabla)\vec{U} = -\nabla p + \frac{1}{Re}(\nabla^2 \vec{U}), \tag{2}$$

$$\nabla . U = 0. \tag{3}$$

One of the main difficulties in the solving the Navier-Stokes equations are the lack of information about the pressure at the boundaries. This is overcome by either using the staggered grid for the discritization or by eliminating the pressure term from the Navier-Stokes equations. Application of the following vector identity:

$$\begin{array}{l} \nabla(A.B) = (B.\nabla)A + (A.\nabla)B + \\ B \times (\nabla \times A) + A \times (\nabla \times B) \end{array} . \tag{4}$$

for the case of $A = B = \vec{U} = (U, V, W)$ results in the formation of Eq. (5)

$$(\vec{U}.\nabla)\vec{U} = \vec{\omega} \times \vec{U} + \frac{1}{2}\nabla(\vec{U}.\vec{U}) \tag{5}$$

where $\vec{\omega} = (\omega_1, \omega_2, \omega_3) = \nabla \times U$. If Eq. (5) is substituted for the convective term in the non-dimensionalized Navier-Stokes equation (Eq. (2)), it gives:

$$\frac{\partial \vec{U}}{\partial t} = \vec{H} - \nabla(p + \frac{\vec{U}.\vec{U}}{2}) + \frac{1}{Re}(\nabla^2 \vec{U}) \tag{6}$$

where $\vec{H} = (H_1, H_2, H_3) = \vec{U} \times \vec{\omega}$. Taking $\nabla \times$ (6) results in

$$\frac{\partial(\nabla \times \vec{U})}{\partial t} = \nabla \times \vec{H} - \nabla \times \nabla(p + \frac{\vec{U}.\vec{U}}{2}) + \frac{1}{Re}\nabla^2(\nabla \times \vec{U}) \tag{7}$$

which will further simplify to Eq. (8) on the usage of $\nabla \times \nabla\,(scalar) = 0$.

$$\frac{\partial \vec{\omega}}{\partial t} = \nabla \times \vec{H} + \frac{1}{Re}\nabla^2 \vec{\omega}. \tag{8}$$

By taking $\nabla \times$ (8), the following equation will be obtained.

$$\frac{\partial \nabla \times (\nabla \times \vec{U})}{\partial t} = \nabla \times (\nabla \times \vec{H}) + \frac{1}{Re}\nabla^2(\nabla \times (\nabla \times \vec{U})). \tag{9}$$

Using the continuity equation ($\nabla.\vec{U} = 0$) and applying the next vector identity

$$\nabla \times (\nabla \times \vec{U}) = \nabla(\nabla.\vec{U}) - \nabla^2 \vec{U} \tag{10}$$

converts Eq. (9) into the following equation

$$\frac{\partial \nabla^2 \vec{U}}{\partial t} = \nabla \times (\nabla \times \vec{H}) + \frac{1}{Re} \nabla^4 \vec{U}. \tag{11}$$

Where the vector $\vec{H} = \vec{U} \times \vec{\omega}$ contains the non-linear terms and $Re = \Delta U \delta_\omega / \nu$. Equations (8) and (11) are the evolution equations responsible for the time-advancement in the simulation.
The instantaneous velocity $U = (U, V)$ is decomposed into a base flow $(U_0(y), 0)$ and the computational flow velocity components $(u(x, y, t), v(x, y, t))$ as follow.

$$U(x, y, t) = u(x, y, t) + U_0(y) \ , \tag{12}$$

$$V(x, y, t) = v(x, y, t). \tag{13}$$

Using the streamwise components of Eq. (8) and Eq. (11) and the decomposition shown by Eq. (12) yields:

$$\frac{\partial}{\partial t} \nabla^2 u = \frac{\partial^2}{\partial y^2} H_1 - \frac{\partial^2}{\partial x \partial y} H_2 + \frac{1}{Re} \nabla^4 U, \tag{14}$$

where $\omega_1 = \omega_2 = H_3 = 0$ for the case of two dimensional flow. Eq. (14) and the convective outflow boundary condition are responsible for the time-advancement of the simulation. The cross-stream velocity component v is recovered directly from the continuity equation.

$$\frac{\partial v}{\partial y} = -\frac{\partial u}{\partial x}. \tag{15}$$

The vorticity component ω_3 is calculated following its definition.

$$\omega_3 = \frac{\partial V}{\partial x} + \frac{\partial U}{\partial y}. \tag{16}$$

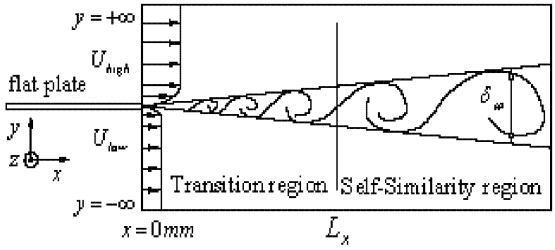

Figure 1. Spatially developing mixing layer geometry [1].

3. Boundary and Initial Conditions

Equation (14) is a fourth-order, partial differential equation, so it requires four boundary conditions. The u velocity is specified at the inlet ($x = 0$) and the outlet boundaries ($x = L_x$). With the help of continuity equation, $\partial u / \partial x$ is also specified at the inflow and outflow boundaries:

$$\frac{\partial u}{\partial x} = -\frac{\partial v}{\partial y}. \tag{17}$$

The former and the latter are known as Dirichlet and Neumann type boundary conditions, respectively. The boundary conditions are set to be zero in the transverse direction.
In the numerical simulations, the instantaneous velocity component at the inlet boundary is specified using tangent hyperbolic profile (Eq. (1)) which is superimposed by some perturbations. The perturbations are introduced in the form of a traveling wave. The perturbation part, which is a combination of linear eigenfunctions obtained from the linear stability calculations, is specified for the inflow boundary condition [15]. In other words:

$$v\left(x,y,t\right)=A\cdot\text{Real}\,\left[V\left(y\right)\,e^{i(-\omega t)}\right] \tag{18}$$

where $V\left(y\right)$ is the velocity eigenfunction corresponding to the most amplified mode of the two-dimensional Orr-Sommerfeld equation and A is the amplitude of the two-dimensional forcing which corresponds to the fundamental frequency.
Convective outflow boundary conditions are specified at the outflow. The boundary conditions must be non-reflective to avoid feedback problem. The convective boundary conditions are used to generate the Dirichlet boundary conditions for both velocity components.

$$\frac{\partial\psi}{\partial t}=-c\frac{\partial\psi}{\partial x}. \tag{19}$$

where ψ is replaced by each of the velocity components. In (19), c represent the advection speed of the large-scale structures in the layer. The purpose of this condition is to allow the fluid structures to flow out of the domain in a natural manner. Therefore, the advection speed is chosen to match the convective velocity of the large spanwise rollers. Experimental studies of the mixing layer have indicated that these large rollers advect downstream at speeds close to that of the mean speed of the layer [15]. Therefore, c was set as $c=\bar{U}=\left[U_1+U_2\right]/2$ (including normalization) for the simulations presented here. Lang [16] has indicated that, while the large scale structures appear to advect at approximately the average of the free stream speeds, c, the small scale structures move with a different speed – something close to the local mean speed of the layer. For the low Reynolds number flows simulated in this work the small-scale structures are, in fact, relatively large. Moreover, the results indicate that the region of the influence of the outflow boundary condition is restricted to a fairly short distance upstream of the exit plane-roughly one layer thickness. Therefore, the choice of $c=\bar{U}$ is appropriate for these simulations as will be evident in the result to outflow.
An unforced, two-dimensional mixing layer simulation whose inlet boundary contains a base profile (Tangent hyperbolic mean velocity distribution), provided the initial conditions for the forced mixing layer simulations.
A uniformly distributed Tangent hyperbolic mean velocity at all x stations is the initial condition for the unforced two-dimensional mixing layer simulation. These initial conditions must then be allowed to wash out before performing any statistical analysis on the layer. In other words, any particle at the inlet ($x=0$) must be allowed to leave the outlet boundaries ($x=L_x$). The mixing layer flow must also reach the statistically stationary state in which the mean velocity component is time independent

4. Numerical Formulation

The spatially developing mixing layer is solved in a domain with a finite extend in the streamwise direction and doubly infinite ($y \to \pm\infty$) in the major-gradient (MG) direction. A mapping is employed to convert the doubly-infinite y extend of the original domain into a computational domain of ζ with interval $-1 \leq \zeta \leq 1$. Equations (14), (15) and (16) indicate that for each time step (sub time step) a method is required that can:

- evaluate the spatial derivatives,
- integrate the continuity equation to recover v from Eq. (15),
- compute the non-linear terms in Eq. (14),
- solve the two dimensional Poisson equation for u.

At the end of each time step the solution can be regarded as a new initial condition for u. This is required for time-advancement of the computations.

4.1. Streamwise Derivatives. The derivatives in the streamwise direction are computed using the Pade' finite difference scheme developed by Lele [17], [18]. He introduced the first derivative of $f(x)$ implicitly according to

$$\alpha f'_{j-1} + f'_j + \alpha f'_{j+1} = \tfrac{\alpha+2}{3h}(f_{j+1} - f_{j-1}) + \tfrac{4\alpha-1}{12h}(f_{j+2} - f_{j-2}) \tag{20}$$

where a prime denotes the first derivative, j represents the grid number ($0 \leq j \leq J$) and $h = \Delta x = Lx/J$. By setting $\alpha = 1/4$ or $\alpha = 1/3$ a fourth-order or sixth-order accurate scheme is obtained. At the stramwise boundaries (e.g. at $j = 0$ and $j = J$) an implicit one-sided, third-order derivative approximation is used:

$$f'_0 + 2f'_1 = \frac{1}{2h}(-5f_0 + 4f_1 + f_2), \tag{21}$$

$$f'_J + 2f'_{J-1} = \frac{1}{2h}(5f_J - 4f_{J-1} - f_{J-2}). \tag{22}$$

At the vicinity of the boundaries (e.g. at $j = 1$ and $j = J - 1$) the general form of the first derivatives (Eq. (20)) is used with $\alpha = 1/4$. Lele [17] discussed that replacing of α by $\alpha' = (16\alpha + 32)/(40\alpha - 1)$ at $j = 2$ and $j = J - 2$ guarantees the stability and numerical conservation of $(\partial/\partial t)\, u = (\partial/\partial x)\, f\,(u)$. Figure (2) shows the accuracy of the Pade' finite difference scheme for the first derivatives of $y = 3\sin(2x) + x^2$.
The Pade' finite difference scheme, as introduced above, is an implicit scheme. It is expected to realize a third order accurate scheme at the boundaries and a sixth order accurate scheme far from both boundaries (e.g. at $x = L_x/2$). Figure (3) shows the order of accuracy [19].
Equation (23) represents the second derivative of $f(x)$, which is the family of fourth order accurate Pade' finite difference schemes.

$$\alpha f''_{j-1} + f''_j + \alpha f''_{j+1} = \tfrac{4(1-\alpha)}{3h^2}(f_{j+1} - 2f_j + f_{j-1}) + \tfrac{10\alpha-1}{12h^2}(f_{j+2} - 2f_j + f_{j-2}) \tag{23}$$

where $\alpha = 1/4$. At the boundaries, one-sided, third order scheme are used. They are:

$$f''_0 + 11f''_1 = \frac{1}{h^2}(13f_0 - 27f_1 + 15f_2 - f_3) \tag{24}$$

and

$$f''_J + 11f''_{J-1} = \frac{1}{h^2}(13f_J - 27f_{J-1} + 15f_{J-2} - f_{J-3}). \tag{25}$$

Taking the first order derivative from both sides of Eq. (21) gives

$$f''_0 + 2f''_1 = \tfrac{1}{2h}(-5f'_0 + 4f'_1 + f'_2) = \tfrac{-3}{h}f'_0 + \tfrac{1}{2h}(f'_0 + 4f'_1 + f'_2)\ . \tag{26}$$

Substituting the left-hand-side of Eq. (21) (using $\alpha = 1/4$) for the terms in the parenthesis of Eq. (26) forms the following equation.

$$f''_0 + 2f''_1 = \frac{-3}{h}(\frac{df}{dx})_{x=0} - \frac{3}{2h^2}(f_0 - f_2). \tag{27}$$

Equation (27) is used at the inlet boundary when both the function value and its derivative are known. An analogous approach is performed to specify the second derivative at the outflow boundary when both function value and first derivatives are available.

$$f''_J + 2f''_{J-1} = \frac{3}{h}(\frac{df}{dx})_{x=Lx} - \frac{3}{2h^2}(f_J - f_{J-2}). \tag{28}$$

In the immediate vicinity of the boundaries (at $j = 1$ and $j = J - 1$), the second-order compact finite difference scheme Eq. (23) is used with $\alpha = 1/10$. An evaluation of the fourth derivative, which appears in the biharmonic term of Eq. (14), is performed by imposing the second order derivative operator twice in succession. Figure (4) shows the accuracy of the Pade' finite difference scheme for the second derivatives of $y = 3\sin(2x) + x^2$. Figure (5) shows the order of accuracy for the second order Pade' finite difference scheme at the boundaries and at $x = L_x/2$ [19]. The compact finite difference scheme is an implicit scheme; hence the highest order of accuracy can be obtained at the maximum distance from both boundaries where the lower order schemes are used [20], [21].

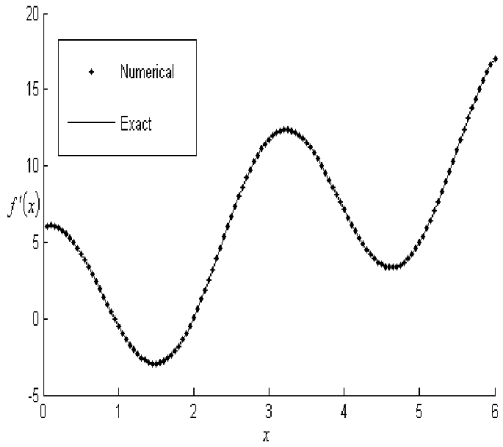

Figure 2. First derivative approximation of $y = 3\sin(2x) + x^2$ using sixth order Pade' finite difference scheme.

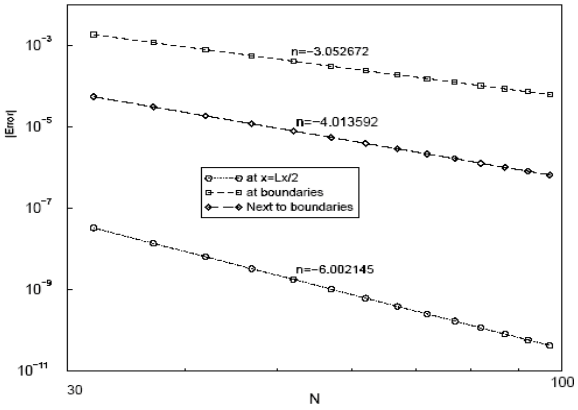

Figure 3. Order of accuracy for first derivative approximation using Pade' finite difference scheme [19].

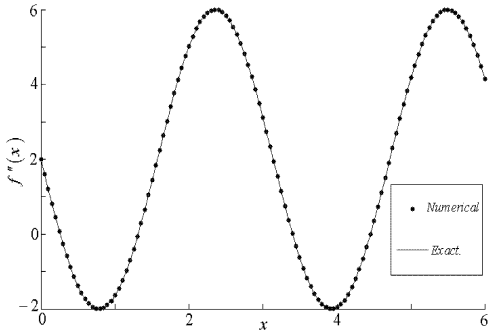

Figure 4. Second derivative approximation of $y = 3\sin(2x) + x^2$ using sixth order Pade' finite difference scheme.

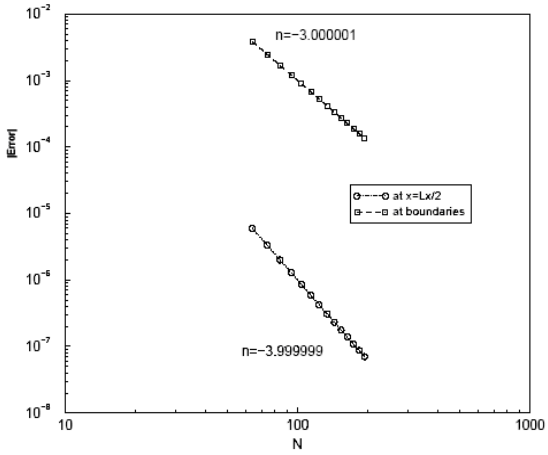

Figure 5. Order of accuracy for second derivative approximation using Pade' finite difference scheme [19].

4.2. Cross-Stream Derivatives. A tangent mapping given as

$$y = \beta \tan(\pi\zeta/2) \tag{29}$$

is used to map the doubly infinite physical domain $-\infty \leq y \leq \infty$ into a finite computational domain with the interval of $-1 \leq \zeta \leq 1$. β in Eq. (29) is a stretching parameter of the mapping. The grid spacing in the computational domain are equally spaced, thus we can directly apply the compact finite difference scheme of Lele [17], [18] to compute the derivatives in the computational domain. However, we must use the chain rule of differentiation to find the derivative in y. Application of the chain rule for the first derivative result in Eq. (30)

$$\frac{df}{dy} = \frac{df}{d\zeta} \times \frac{d\zeta}{dy} = \frac{2}{\pi\beta}\cos^2(\pi\zeta/2)\frac{df}{d\zeta}. \tag{30}$$

By setting $\lambda_1 = \frac{2}{\pi\beta}\cos^2(\pi\zeta/2)$, we have:

$$\frac{df}{dy} = \lambda_1 \frac{df}{d\zeta}. \tag{31}$$

An analogous approach is performed to specify the second derivative

$$\frac{d^2f}{dy^2} = \lambda_2 \frac{d^2f}{d\zeta^2} + \lambda_3 \frac{df}{d\zeta} \tag{32}$$

where

$$\lambda_2 = \lambda_1^2 \tag{33}$$

$$\lambda_3 = -\frac{4}{\pi\beta^2}\sin(\pi\zeta/2)\cos^3(\pi\zeta/2) \tag{34}$$

The accuracy of the numerical code used to calculate the first and second derivatives of $f(y) = \exp\left(-\gamma y^2\right)$, where $\gamma = 1$, is checked against the exact derivatives. The results, shown in Figs (6) and (7), indicate excellent approximations for the cross-stream derivatives.

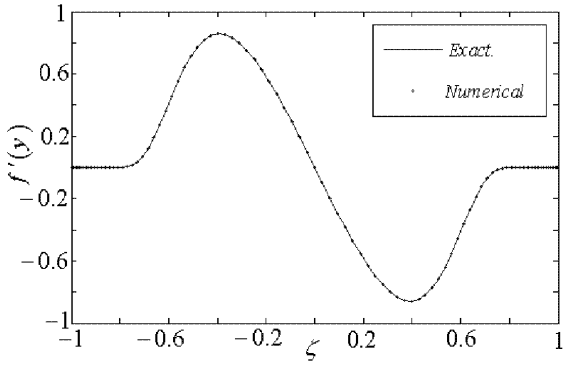

Figure 6. First derivative approximation in cross stream direction for $f(y) = e^{-\gamma y^2}$ with $\gamma = 1, \beta = 1$.

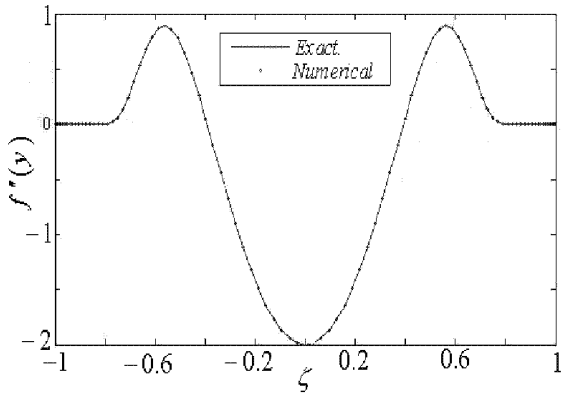

Figure 7. Second derivative approximation in cross stream direction for $f(y) = e^{-\gamma y^2}$ with $\gamma = 1, \beta = 1$.

4.3. Integrating of the Continuity Equation. Equation (15) is the governing equation for the cross-stream velocity. Using the compact finite difference scheme, indicate that the right-hand-side (RHS) of equation (20) experience the ill-conditioning problem. In other words the diagonal elements of RHS matrix of Eq. (20) are zero. To overcome ill-conditioning problem the y derivative operator is applied on both sides of Eq. (15).

$$\frac{\partial^2 v}{\partial y^2} = -\frac{\partial^2 u}{\partial x \partial y}. \tag{35}$$

Equation (35) is not ill-conditioned. This also satisfies the boundary conditions at infinities. In other words Eq. (35), which is second order differential equation, is solved with $v\,(y = \pm\infty) = 0$ as boundary conditions.

4.4. Solution of the Poisson Equation. The application of the time advancement scheme to Eq. (14) generates a Poisson equation for $\Delta u\,(x, y)$.

$$\nabla^2 \Delta u = \frac{\partial^2 \Delta u}{\partial x^2} + \frac{\partial^2 \Delta u}{\partial y^2} = C \tag{36}$$

where C is the linear combination of the RHS of (14). Substituting the second derivatives operators in x and y directions gives

$$(D2X.\Delta u^T)^T + D2Y.\Delta u = C. \tag{37}$$

Eq. (37) can be written in the following form.

$$\Delta u.D2X^T + D2Y.\Delta u = C. \tag{38}$$

Thus, the direct solution of Eq. (36), using a Pade' finite difference scheme for the second derivatives in x and y, forms a matrix equation of the form $AZ + ZB = C$. Bartlez [22] has solved the matrix equation $AZ+ZB = C$. Note that here $A = D2Y$, $B = D2X^T$ and $Z = \Delta u$.

4.5. Time Advancement Scheme. A compact, third order, Runge-Kutta time differencing scheme developed by Wray [23] is used to advance the computations in time. Application of the time advancement scheme to the following model equation

$$\frac{\partial u}{\partial t} = R(u) \tag{39}$$

is performed in three sub-steps according to table (1). The table shows that the time advancement of Eq. (39) by one time increment (Δt) requires computation of the right-hand-side (R) in three successive sub-time-steps. In each of these sub-steps, time (t) is incremented by $(c_i + d_i)\Delta t$ and u is accumulated by linear combination of (R) associated with the current time level and that of the previous sub-time-step. Results in the second column of the third sub-time-step are regarded as the solution of the model equation at next time step. In other words, it is the solution incremented by (Δt).
The coefficient used in the time advancement scheme (c_i, d_i) can be obtained using the Taylor series for $R^{'}$ and $R^{"}$ and equating the terms of like orders. This leads to:

$$c_1 + c_2 + c_3 + d_1 + d_2 + d_3 = 1,$$

$$c_1^2 c_2 + c_3(c_1 + c_2(1 + \frac{d_2}{c_2}))^2 + c_1^2 d_3 = 1/3,$$

$$c_1 c_2 + c_3(\frac{d_2}{c_2}(1 + \frac{d_3}{c_3}) + c_2(1 + \frac{d_2}{c_2})) = 1/2,$$

$$c_1 c_2 c_3 = 1/6.$$

There are two parameter families of solutions to the preceding set of equations. The scheme will be self-starting if $d_1 = 0$. One parameter families of solution to the set of equations is:

$d_1 = 0,$	$c_1 = 8/15,$
$d_2 = -17/60,$	$c_2 = 5/12,$
$d_3 = -5/12.$	$c_3 = 3/4,$

A test case is performed to verify the order of accuracy for the time advancement scheme. The equation

$$du/dt = -u(t) \tag{40}$$

has an exact solution of $u(t) = e^{-t}$ when the initial condition is set to $u\,(0) = 1$. Hence, the right hand side of Eq. (40) and the initial condition $u\,(0) = 1$ are used to solve for $u(t)$ at $t = 1$ using different time increment. The maximum errors between the numerical results and the exact solution are shown in Fig. (8) which clearly indicates that the order of accuracy is approximately three [10].

Table1. Runge-Kutta time advancement scheme

Time	1st location	2nd location
t^n	u^n	$R(u^n)$
$t' = t^n + c_1\Delta t$	$u' = u^n + c_1\Delta t R$	$R' = R(u')$
$t'' = t' + (c_2 + d_2)\Delta t$	$u'' = u' + (c_2 R' + d_2 R)\Delta t$	$R'' = R(u'')$
$t^{n+1} = t^n + \Delta t$	$u^{n+1} = u'' + (c_3 R'' + d_3 R')\Delta t$	

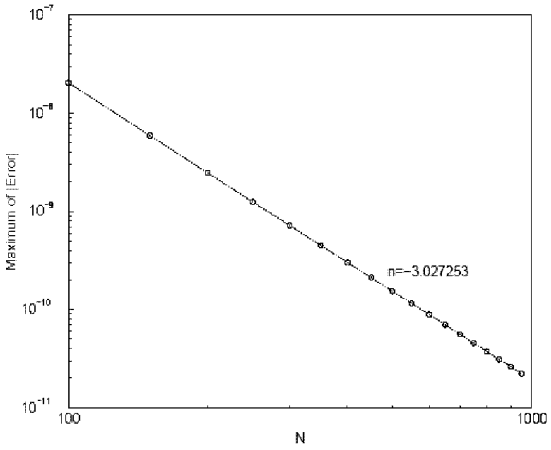

Figure 8. Order of time advancement scheme for $du/dt = -u(t)$ with $u(0) = 1$ [19].

5. Code Verification

The verification of the code was performed with two test cases. They are the two dimensional time dependant diffusion equation and the two dimensional Stuart solution.

5.1. Time Dependant Diffusion Equation. This test case concerned solving the two dimensional, time dependant scalar diffusion equation,

$$\frac{\partial \psi}{\partial t} = \nu \left(\frac{\partial^2 \psi}{\partial x^2} + \frac{\partial^2 \psi}{\partial y^2} \right) \tag{41}$$

on the domain $0 \leq x \leq L_x = 2\pi/3$ and $-\infty \leq y \leq +\infty$. The boundary conditions imposed in this problem were,

$$\frac{\partial \psi}{\partial t}|_{x=0} = \frac{\partial \psi}{\partial t}|_{x=L_x} = 0, \tag{42}$$

and

$$\frac{\partial \psi}{\partial y}|_{y \to \pm\infty} = \psi\,(x, y, t)\,|_{y \to \pm\infty} = 0. \tag{43}$$

The initial condition imposed on ψ was as follows:

$$\psi\,(x,y,0) = \sin\,(2\pi x/L_x)\;\; e^{-y^2}. \tag{44}$$

The generic dependant variable, ψ, has been used in this problem to reflect the fact that the problem was solved for each of the regular flow field $u\,, v$ simultaneously during the test. This allows verification of the time advance and diffusion operator section of the code for each dependant variable.
The problem was solved for the case of $\nu = 1/100$. The problem domain discretized with the following number of nodes and stretching parameter:
$N_x = 45$, $N_y = 40$ and $\beta = 4$.
The computation run for 2000 time steps at which the numerical solution was compared with the analytical solution of (41). That is:

$$u(x,y,t) = \cos(x) \times \frac{y-1}{(1+\frac{4t}{Re})^{1.5}} \times \exp(-2t/Re) \times \exp(-\frac{(y-1)^2}{(1+\frac{4t}{Re})}) \;\; . \tag{45}$$

The maximum errors between the numerical results and the exact solution are shown in Fig. (9).The uniform decay of the solution is evident from this plot. Clearly, the error is within acceptable bounds thereby corroborating the validity of the time advancement and the computation of the diffusion part of the code.

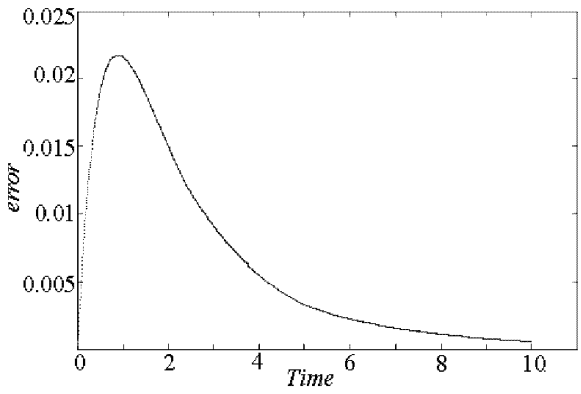

Figure 9. Error analysis for u in time dependant diffusion equation.

5.2. Stuart Solution. Stuart [24] provides a class of exact solution to the inviscid Navier-Stokes equations which simulate two dimensional mixing layer flow. The particular solution of interest here has, as its foundation, a tanh profile for the u velocity component. As a consequence, the flow is periodic in the x direction and advects downstream at the mean speed of the layer, c. The analytical expression for the stream function, ψ (not to be confused with the generic dependant variable of the previous subsection), is:

$$\psi(x,y,t) = cy + \ln(a\cosh(y-y_0) + b\cos(x-ct)) \tag{46}$$

where $b = \sqrt{a^2-1}$. The velocity components u and v, as well as the vorticity component ω_z, are obtained by differentiating this expression with respect to x and y as appropriate. These are:

$$u = \frac{\partial \psi}{\partial y} = c + \frac{a\sinh\,(y-y_0)}{a\cosh\,(y-y_0) + b\cos\,(x-ct)}, \tag{47}$$

$$v = -\frac{\partial \psi}{\partial x} = \frac{b \sin(x - ct)}{a \cosh(y - y_0) + b \cos(x - ct)}, \tag{48}$$

$$\omega_z = \frac{1}{[a \cosh(y - y_0) + b \cos(x - ct)]^2}. \tag{49}$$

The Stuart solution provide an excellent test for the time advancement the formation of the right hand side of Eq.(14) and the advection section of the code. Therefore, the time development of this field was computed for a case with $b = 1/2$ and $c = 1$ on the domain of $0 \leq x \leq L_x = 2\pi/3$ and $-\infty \leq y \leq +\infty$. The domain was discretized using the following number of nodes and stretching parameter: $N_x = 45$, $N_y = 40$ and $\beta = 4$.
Plots of the maximum errors between the numerical results and the exact solution of u and v are shown in Fig. (10).

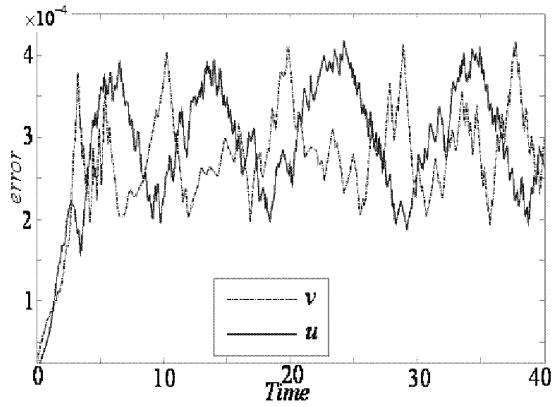

Figure 10. Error analysis for u and v in time dependant Stuart solution.

6. Mixing Layer Simulation

The case of 2D mixing layer was considered in the domain of $0 \leq x \leq 200$ and$-\infty \leq y \leq +\infty$. The velocity ratio for this case,$r = U_2/U_1$, was set at 1/2.This value represents a moderately sheared layer intermediate between the case of a single-stream mixing layer (i.e., $U_2 = 0$) and the splitter-plate wake case ($r = 1$). The average speed of layer,$\bar{U} = 0.5(U_1 + U_2)$, was 1.5. The Reynolds number,$Re_{\delta_{\omega 0}} = \Delta U \delta_{\omega_0}/\nu$, is set at 300. The domain was discretized using 1024 points to represent the streamwise (x) extend of the domain; 256 collocation points were used to represent the MG direction. A time step of 0.05 was used in this work. In the absence of external forcing, the results of the simulation display essentially laminar growth at the Reynolds number described above. Figure (11) illustrates the streamwise growth of the vorticity thickness, $\delta_\omega = 1/\left(\partial \bar{u}/\partial y\right)_{\max}$ for this case. A square-root relationship fit to these computed results is shown in the figure. The layer is responded with the classical laminar, square-root growth characteristics. This is evident by the close agreement indicated by the computed results. The slight deviation from this square-root behavior near the exit plane is explained a result of the artificiality of the outflow boundary condition applied at $x = 200$.
The mean field statistics for the streamwise velocity component and vorticity are illustrated in Figures (12) and (13). Clearly, these results are representative of a self-similar layer.

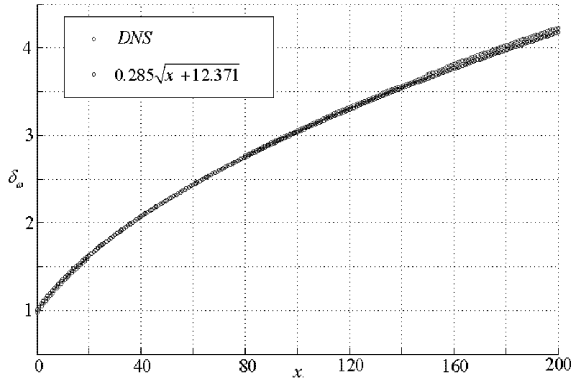

Figure 11. Streamwise growth of the vorticity thickness for the unperturbed layer. Curve fit using $\delta_\omega = a\sqrt{x - x_0}$ with $a = 0.2875$ and $x_0 = -12.371$

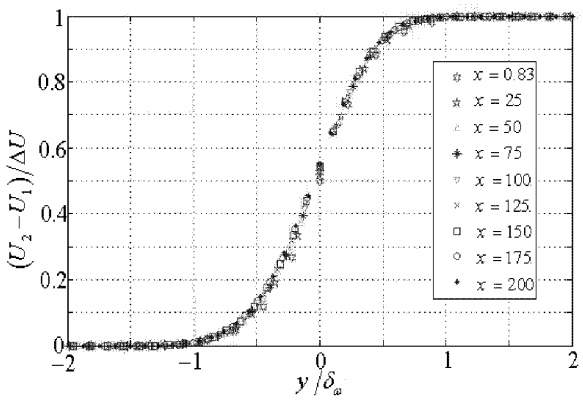

Fig 12. Mean field statistics for $\left(\bar{U} - U_2\right) \Big/ \Delta U$.

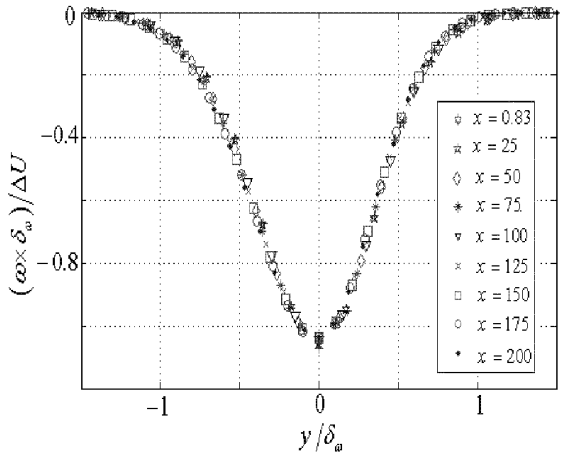

Fig13. Mean field statistics for $(\omega \times \delta_\omega) / \Delta U$.

7. Forced Mixing Layer

The case of forcing considered in this investigation applies a set of time dependant perturbations to the v velocity component at the inlet plane. These perturbations are generated by the means of linear stability analysis for the most unstable mode. Figure (14) provides a snapshot of the vorticity field at the simulation. Sufficient time has been elapsed for the initial, start up field to have washed-out of the computational domain. Note the presence of two pairing regions is evident in this figure. The structures evident in this figure are advected downstream at approximately the mean speed of the layer, $\bar{U}$. Figure (15) compares the computed streamwise growth of the vorticity thickness, with the laminar growth of vorticity thickness.
Note that, the inflow perturbation has strong influence on the growth of the mixing layer. Suitably selected initial conditions can enhance the growth of the mixing layer [12].
Figures (16) through (20) illustrate time traces of the results for the velocity components at selected location in the layer. The figures clearly indicate that the response of the layer is very periodic. This is due to the periodic forcing imposed at the inlet plane of the layer.
The peak-to-peak time lapse in these curves provides evidence of the passage of a structure. This time laps, Δt, together with an assumed advection speed for these structures of $\bar{U}$, allows estimation of the scale of a structure.
The mean field statistics for each of the velocity components and vorticity are illustrated in figures (21) through (23). Clearly, these results are not representative of a self-similar layer. The lack of self-similarity is very evident in the plot of v and ω. This is apparently as a result of the forcing imposed at the inlet plane. As the flow goes downstream, the distributions become closer together. This is indicating that the flow enters the self-similar region.

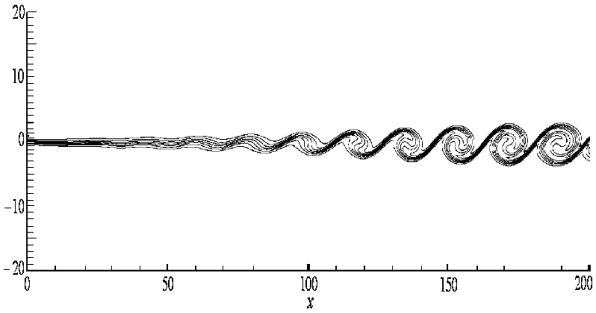

Figure 14. Snapshots of the results for ω_z.

The turbulence intensities realized for the velocity components in this simulation are presented in Fig (24) and (25). Again, these statistical quantities indicate that the layer is not self-similar in the near field regions. The curve representing the turbulence intensity of the u component (Fig. (24)) are very different in the shape from those of the self-similar layer. Figure (25) illustrates the turbulence intensity for the v component. The shape of these profiles is more like that of the self-similar layer than for the u component. The peak intensity for this component exceeds to that of the u component.
The Reynolds stress statistics obtained from this simulation are illustrated in Fig. (26). Again, these profiles do not exhibit self-similar behavior. The distributions are more likely collapse on each other at far downstream of the flow.

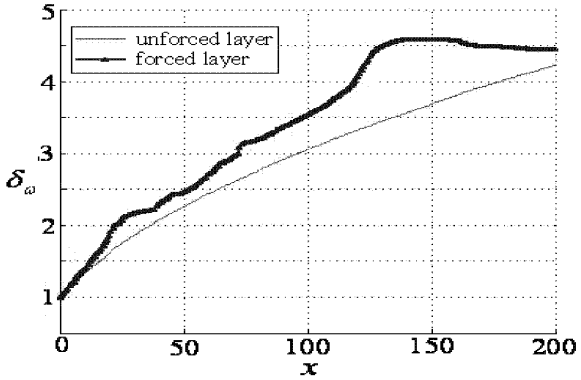

Figure 15. streamwise development of the vorticity thickness in forced layer.

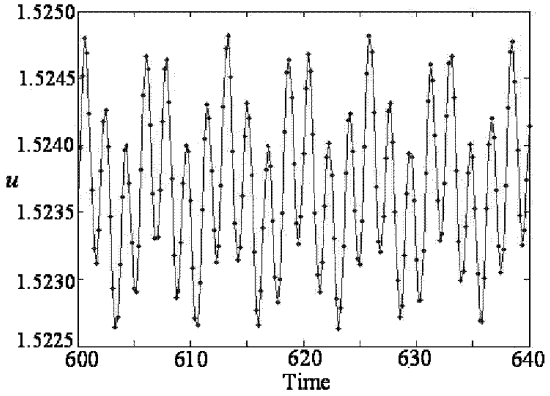

Figure 16. Velocity time histories for the u component at streamwise location $x = 50$.

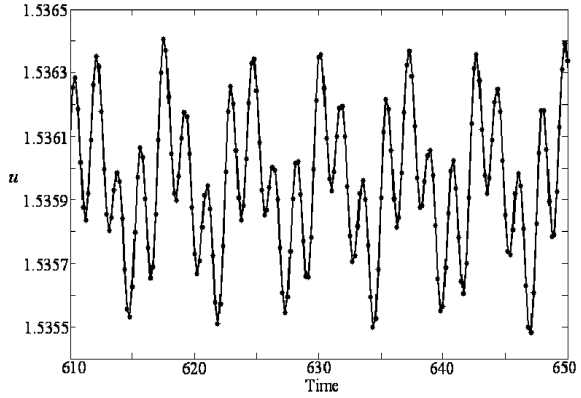

Figure 17. Velocity time histories for the u component at streamwise location $x = 100$.

8. Conclusion

The two dimensional incompressible, spatially developing, forced plane mixing layer has been simulated in this work. A numerical method which employs a combination of compact finite difference and a mapped compact finite difference scheme are

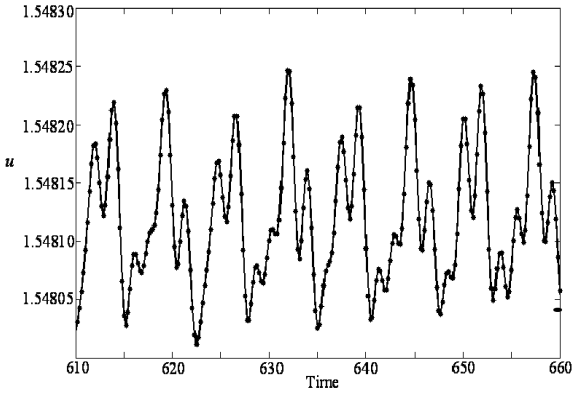

Figure 18. Velocity time histories for the u component at streamwise location $x = 200$.

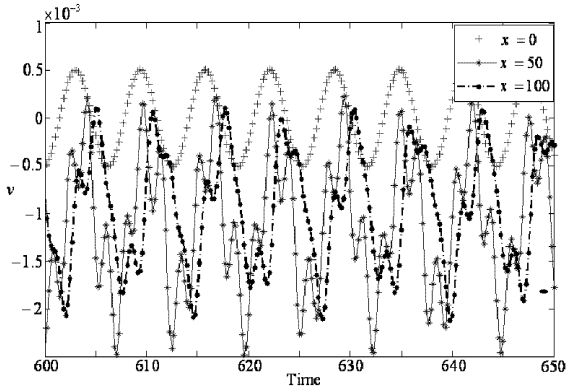

Figure 19. Velocity time histories for the v component at streamwise locations $x = 0, 50, 100$.

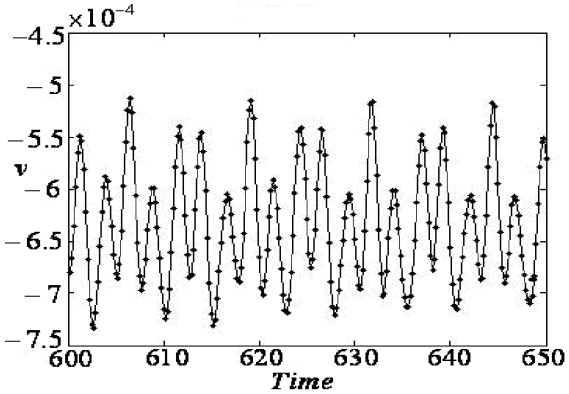

Figure 20. Velocity time histories for the v component at streamwise location $x = 200$.

used to represent the spatial dependence of the mixing layer flow. Compact finite difference were used to represent the solution in the stramwise direction and a mapped compact finite difference method was employed to describe the solution dependence in the major gradient direction. The simulations were time advanced

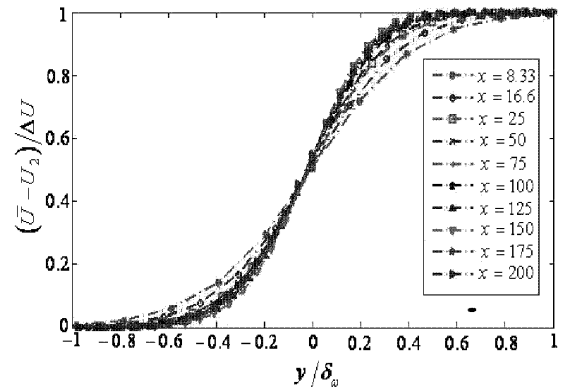

Figure 21. Mean field statistics for $\left(\bar{U}-U_2\right)\Big/\Delta U$.

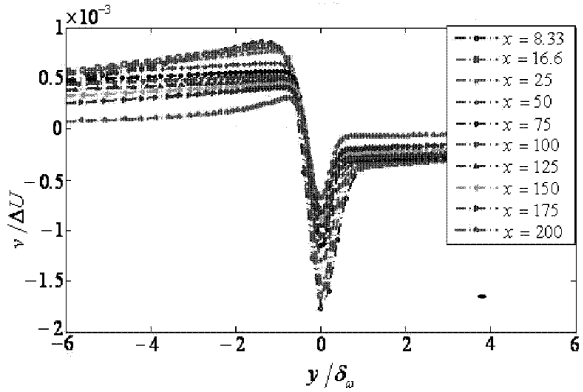

Figure 22. Mean field statistics for $v/\Delta U$.

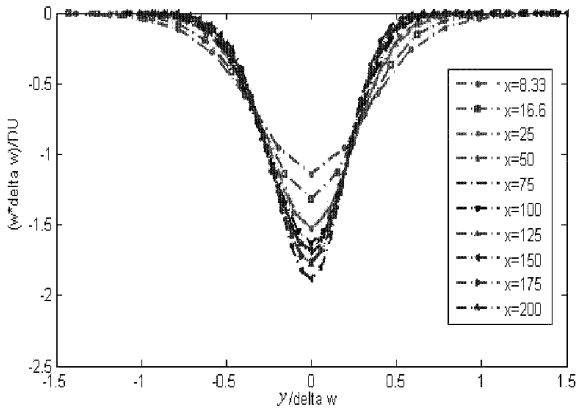

Figure 23. Mean field statistics for $(\omega \times \delta_\omega)/\Delta U$.

by means of a third order Runge-Kutta method. The inflow boundaries are excited to generate the forced mixing layer solutions. An advection type outflow boundary condition was employed in this work. This condition appears to allow a simulation that does no distort the structures as they exit the computational domain. This

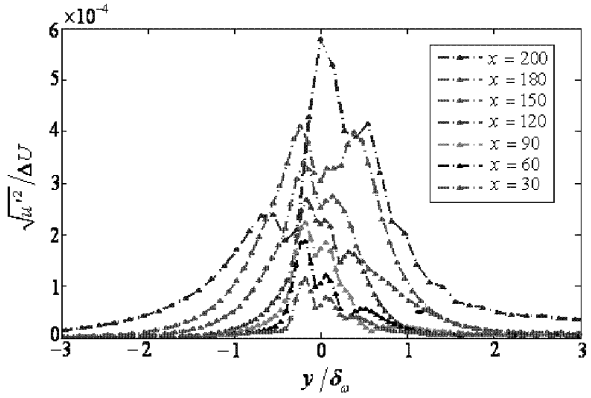

Figure 24. Turbulence intensity for $\sqrt{u'^2}\Big/\Delta U$.

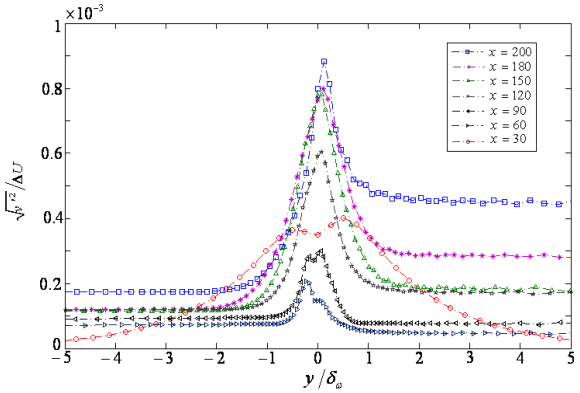

Figure 25. Turbulence intensity for $\sqrt{v'^2}\Big/\Delta U$.

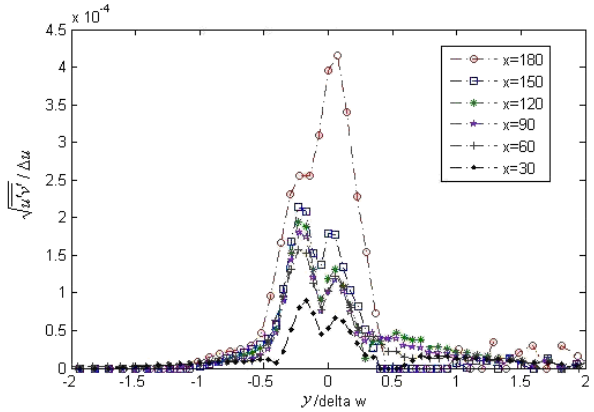

Figure 26. Reynolds stress for $\sqrt{u'v'}\Big/\Delta U$.

simulation reflects the imposition of a time dependant perturbation function at the inlet plane. This perturbation corresponds to the fundamental mode corresponding to solutions to the Orr-Sommerfeld equation for the hyperbolic tangent inviscid shear layer profile. The results of the simulation capture the physics of the forced mixing layer quite well.

References

[1] Pellerin S., Dulieu A., Tenaud C. and Taphuoc C., Evaluation of Time and Space Scales in a Spatially Developing 3D Turbulence Incompressible Mixing Layer by Using LES, 3rd AFOSR International Conference on DNS and LES (TAICDL), August 5-9, 2001.

[2] Schlichting H. and Gersten K., Boundary Layer Theory, Springer-Verlag, 8th ed., 2000.

[3] Liepmann H. and Laufer J., Investigation of Free Turbulent Mixing, NASA TN 1257, 1947.

[4] Brown G., and Roshko A., On Density Effects and Large Structure in Turbulent Mixing Layer, J. Fluid Mech. 1974, 64(4): 775-816.

[5] Mungal M.G and Dimotakis P.E., Mixing and Combustion with Low Release in a Turbulent Shear Layer, J. Fluid Mech.1984, 148: 349-382.

[6] Yang W.B., Zhang H.Q., Chan C.K. and Lin W.Y. Large Eddy Simulation of Mixing Layer, J. Computational and Applied Mathematics, 2004, 163: 311-318.

[7] Tenaud C., Pellerin S., Dulieu A. and Phuoc L. Large Eddy Simulation of a Spatially Developing Incompressible 3D Mixing Layer Using the Formulation, J. Computers & Fluids, 2005, 34: 67-96.

[8] Sagaut P., Large Eddy Simulation of Incompressible Flows. An Introduction, Springer-Verlag, 2001.

[9] Rai M.M. and Moin P., Direct Simulation of Turbulent Flow Using Finite Difference Schemes, J. Comp. Phys., 1991, 96: 15-33.

[10] Moin P. and Mahesh K, Direct Numerical Simulation: A Tool in Turbulence Research, Annu. Rev. Fluid Mech., 1998, 30: 539-578.

[11] Li Q., and Fu S., Numerical Simulation of High-Speed Planar Mixing Layer, J. Computers & Fluids, 2003, 32: 1357-1377.

[12] Hu Zh., Luo X. and Luo K.H. Numerical Simulation of Particle Dispersion in a Spatially Developing Mixing Layer, J. Theoretical & Computational Fluid Dynamics, 2002, 15: 403-420.

[13] Michioka T., Kurose R., Sada K. and M H. Direct Numerical Simulation of a Particle-laden Mixing Layer with a Chemical Reaction, International Journal of Multiphase Flow, 2005, 31: 843-866.

[14] Miller R.S., Madnia C.K. and Givi P. Structure of a Turbulent Reacting Mixing Layer, J. Combustion Science & Technology, 1994, 99(1-3): 1-36.

[15] Lowery P.S. and Reynolds W., Numerical Simulation of Spatially Developing, Forced, Plane Mixing Layer, NASA Technical Report NCC2-015, 1986.

[16] Lang D.B., Laser Doppler Velocity and Vorticity Measurements in Turbulent Shear Layers, AIAA paper, 1985, 83-0475.

[17] Lele S.K., Compact Finite Difference Scheme with Spectral-Like Resolution, Journal of Computational Physics, 1992, 103: 16-42.

[18] Lele S.K., Ferziger, J.H., A High Order Compact Method for Large Eddy Simulation, Journal of Computational Physics, 2003, 191:392-419.

[19] Maghrebi M.J. A Study of the Evolution of Intense Focal Structures in Spatially-Developing Three-Dimensional Plane Wake, PhD thesis, Department of Mechanical Engineering, Monash University, Melbourne, Australia, 1999.

[20] Mahesh K., A Family of High Order Finite Difference Schemes with Good Spectral Resolution, Journal of Computational Physics, 1998, 45:332-358.

[21] Rizetta D.P., Visbal M.R., Morgan P.E., A High Order Compact Finite Difference Scheme for Large Eddy Simulation of Active Flow Control, Progress in Aerospace Science, 2008, 44:397-426.

[22] Bartles R.H. and Stewart G.W. Solution of the Matrix Equation AX+XB=C, Communications of the ACM, 1972, Vol 15, Number 9.

[23] Wray A., and Hussaini M.Y. Numerical Experiments in Boundary Layer Stability, Proc. R. Soc. Lond, 1984, 392: 373-389.

[24] Stuart J.T. On Finite Amplitude Oscillations in Laminar Mixing Layer, J. Fluid Mech., 1967, 29: 417-440.

Department of Mechanical Engineering, Shahrood University of Technology, Shahrood, Iran
E-mail: Javad@shahroodut.ac.ir and Ahad.Zarghami@gmail.com